Chapter in the *Solar System Beyond Neptune* book, U. Arizona Press, Space Science Series, 2008

Physical Effects of Collisions in the Kuiper Belt

Zoë M. Leinhardt and Sarah T. Stewart
Harvard University

Peter H. Schultz
Brown University

Collisions are a major modification process over the history of the Kuiper belt. Recent work illuminates the complex array of possible outcomes of individual collisions onto porous, volatile bodies. The cumulative effects of such collisions on the surface features, composition, and internal structure of Kuiper belt objects (KBOs) are not yet known. In this chapter, we present the current state of knowledge of the physics of cratering and disruptive collisions in KBO analog materials. We summarize the evidence for a rich collisional history in the Kuiper belt and present the range of possible physical modifications on individual objects. The question of how well present-day bodies represent primordial planetesimals can be addressed through future studies of the coupled physical and collisional evolution of KBOs.

1. INTRODUCTION

The Kuiper belt contains some of the least-modified material in the solar system. Some Kuiper belt objects (KBOs) may be similar to the planetesimals that accreted into the larger bodies in the outer solar system. However, KBOs have suffered various modification processes over the lifetime of the solar system, including damage from cosmic rays and ultraviolet radiation, sputtering and erosion by gas and dust in the interstellar medium, and mutual collisions (e.g., *Stern,* 2003). Robust interpretations of the surfaces and internal structures of KBOs require improved insight into the relative weight of each of these processes.

The present understanding of the importance of collisions on the physical evolution of KBOs is limited by the state of knowledge in three fundamental areas: (1) the dynamical history of the different populations within the transneptunian region (see chapter by Morbidelli et al.); (2) the physical properties of KBOs (chapters by Brown and by Stansberry et al.); and (3) how the physical properties of KBOs (expected to be icy and porous) affect the outcome of collisions (this chapter). The dynamical history of a population defines the evolution of mean impact parameters (velocity, angle, mass ratio of the projectile and the target) within and between KBO populations. The impact parameters and the material properties of the colliding bodies determine the outcome of an individual impact event. Finally, the cumulative effects of collisions are determined by the coupled physical and dynamical evolution of KBOs.

Variable progress has been made in these three areas. Over the past decade, great improvements in observations and models have illuminated the rich dynamical history of the Kuiper belt. At present, there is a sparse but growing body of data on the physical properties of KBOs (e.g., size, density, composition, and internal structure). Although a significant body of work has been devoted to collisions between icy, porous bodies, our understanding of the governing physics is still incomplete. The collisional evolution of KBOs is a particularly interesting and challenging problem because of the range of possible outcomes that depend on the changing dynamical structure of the Kuiper belt.

In this chapter, we present a summary of the work to date that can be applied to the physical effects of collisions in the Kuiper belt. We begin with observational evidence for significant past and present-day collisions in the Kuiper belt (section 2). We then present a range of possible outcomes from collisions between KBOs (section 3) and discuss the principal discriminating factors (section 4). Based on the expected physical properties of KBOs, we summarize the results of laboratory and numerical experiments that have been conducted to determine how material properties, such as composition, porosity, and impact conditions, including velocity and mass ratio, affect collision outcomes (section 5). Finally, we discuss several open questions and future research directions for studying collisions in the Kuiper belt (section 6).

2. EVIDENCE FOR A RICH COLLISIONAL HISTORY IN THE KUIPER BELT

In this section, we summarize four observations that support a significant collisional history within the Kuiper belt. First, we discuss observations of interplanetary dust particles (IDPs) by the Pioneer and Voyager spacecraft (section 2.1). Analyses of the orbits of IDPs conclude that the Kuiper belt must be one of the dust source regions. Second, the size distribution of KBOs has at least one break from a simple power law around diameters of tens of kilometers, which is consistent with models of collisional equilibrium among the smaller bodies (section 2.2). Third, the discovery of a possible dynamical family of objects in the Kuiper belt implies conditions that produced at least one

near-catastrophic collision of one of the largest KBOs (section 2.3). Finally, models of the accretion of the largest KBOs demonstrate that the mass in the ancient Kuiper belt must have been much larger than observed today. The total mass loss of >90%, and perhaps as much as 99.9%, was driven by a combination of dynamical perturbations and collisional grinding (section 2.4).

In addition to the observable features discussed below, collisions within a small body population will also affect rotation rates, surface colors, and the formation of binaries. The rotation rates of bodies in collisional equilibrium will reflect the angular momentum transfer from typical impact conditions (see, e.g., *Love and Ahrens,* 1997; *Paolicchi et al.,* 2002, for asteroid rotations). The formation of binary KBOs is still a matter of debate. Some binaries seem to have formed via collisions, while others have too much angular momentum for a collision origin (*Margot,* 2002). The observed color diversity in the Kuiper belt is also controversial and not correlated directly with collision energy (see chapter by Doressoundiram et al.). However, the range of outcomes from collisions depends on material properties as well as the impact parameters. The growing data on rotation rates, colors, and binaries will provide in the future additional constraints on the collisional evolution in the Kuiper belt.

2.1. Interplanetary Dust Particles

Dust and small meteoroids were detected in the outer solar system by the Pioneer 10 and 11 and Voyager 1 and 2 missions (*Humes,* 1980; *Gurnett et al.,* 1997). Pioneer 10 and 11 measured the concentration and orbital properties of dust from 1 to 18 AU. The dust impacts detected by Pioneer 11 between 4 and 5 AU were determined to have either high inclination or eccentricity or both. In other words, the IDPs were either not on circular orbits and/or not on near-planar orbits. Hence, the observed increase in particle flux at Jupiter could not be explained by gravitational focusing, which is inefficient for highly inclined and eccentric orbits, and *Humes* (1980) suggested that the dust had a cometary origin.

In a reanalysis of the Pioneer data, *Landgraf et al.* (2002) found that the dust flux was relatively constant at distances exterior to Jupiter's orbit. To produce a constant dust flux from drag forces, the dust must originate from a source beyond the detection locations by the spacecraft. *Landgraf et al.* (2002) modeled the radial dust contribution using three source reservoirs, dust from evaporating Oort cloud and Jupiter-family comets and dust from collisions between KBOs, and argue that the amount of dust observed by Pioneer 10 and 11 can only be explained by a combination of all three reservoirs. They find that comets can account for the material detected inside Saturn's orbit but an additional reservoir is necessary for the dust observed outside Saturn's orbit.

Although Voyager 1 and 2 did not carry specialized detectors for dust, *Gurnett et al.* (1997) found that the plasma wave instruments could detect impacts from small particles with masses $\geq 10^{-11}$ g (2–3 orders of magnitude below the mass detection limit by Pioneer 10 and 11). From data collected between 6 and 60 AU, *Gurnett et al.* (1997) found a severe dropoff in dust detection events after 51 AU and 33 AU for Voyager 1 and 2, respectively. As a result, the authors conclude that the source of the dust cannot be interstellar. Furthermore, the small latitudinal gradient decreases the likelihood that the source objects are planets, moons, or asteroids (if the dust did originate from such objects, one would expect a strong latitudinal gradient since the planets, moons, and asteroids are effectively all in the same plane). The Voyager IDP observations are consistent with a dust source from the Kuiper belt (*Gurnett et al.,* 1997; *Jewitt and Luu,* 2000).

In summary, the radial distribution and orbital properties of outer solar system IDPs cannot be explained by source material solely from Jupiter-family comets and Oort cloud comets and indicate the need for an additional active source of dust in the outer solar system. The IDP observations are well matched by models of dust produced during the collisional evolution of the Kuiper belt (e.g., *Jewitt and Luu,* 2000, and section 2.4). Dust derived from mutual collisions in the present day Kuiper belt is analogous to the zodiacal dust from the asteroid belt (*Müller et al.,* 2005) and observations of rings of dust around other main-sequence stars (see chapters by Moro-Martín et al. and Liou and Kaufmann). Because the removal time of dust is much shorter than the age of the solar system (see chapter by Kenyon et al.), the dust must be replenished by collisions occurring throughout the history of the solar system.

2.2. Size Distribution of Kuiper Belt Objects

Formation models indicate that KBOs accreted within a thin disk with low relative velocities and inclinations (see chapter by Morbidelli et al.). However, the present velocity dispersion (~1 km s^{-1}) and the inclination distribution (about 20° half-width) of KBOs are both much higher than expected during the coagulation stage (*Trujillo et al.,* 2001). The large relative velocities and the large inclination distribution of the KBOs point to significant dynamical interactions with Neptune, which resulted in a rich collisional history (*Davis and Farinella,* 1997).

If the bodies in the Kuiper belt were fully collisionally evolved and collision outcomes were independent of size, the differential size distribution ($dN \sim r^{-q}dr$, where N is number of bodies in the size bin of radius r) would be described by a self-similar collisional cascade and fit by a single power-law index of q = 3.5 (*Dohnanyi,* 1969; *Williams and Wetherill,* 1994). If the population is only partially collisionally evolved and/or the disruption criteria is dependent on scale, the size distribution will deviate from a single power law. For example, the size distribution in the asteroid belt deviates from a simple power law in part because of strength effects (*O'Brien and Greenberg,* 2005) and recent collisions, such as dynamical family-forming events (*dell'Oro et al.,* 2001).

Recent observations indicate that the size distribution of KBOs has a break at diameters of tens of kilometers, with

fewer smaller bodies than expected from extrapolation from bodies hundreds of kilometers in diameter (*Bernstein et al.,* 2004; *Chen et al.,* 2006; *Roques et al.,* 2006). The slope of the differential size distribution of large KBOs (<25 mag, >100-km diameter) is well established, with a slope in the range of 4 to 4.8 (*Trujillo et al.,* 2001; *Petit et al.,* 2006; chapter by Petit et al.). *Bernstein et al.* (2004) also suggested that the classical KBOs have a different size distribution from the other dynamical populations (for KBO population classifications, see chapter by Gladman et al.).

Over the past decade, several groups have made significant progress in modeling the collisional evolution of the Kuiper belt (*Davis and Farinella,* 1997; *Stern and Colwell,* 1997; *Kenyon and Bromley,* 2004; *Pan and Sari,* 2005; *Kenyon and Luu,* 1999; chapter by Kenyon et al.). Their work provides a theoretical basis for a break in the KBO size distribution around tens of kilometers. *Davis and Farinella* (1997) first demonstrated that few of the largest bodies in the Kuiper belt experience catastrophic disruption events in which 50% of the mass is permanently removed. In other words, most of the largest KBOs are primordial; they have persisted since the end of the coagulation stage, although some may have suffered shattering collisions.

Collision evolution models indicate that the break in the size distribution corresponds to the upper size limit of the collisionally evolved population (*Davis and Farinella,* 1997; *Kenyon and Bromley,* 2004; *Pan and Sari,* 2005). Over time, collisions preferentially disrupt smaller objects because of their lower critical disruption energies and their higher number densities (and hence higher collision probabilities) compared to larger bodies. When the disruption criteria is size-dependent, the collisionally evolved size distribution deviates from q = 3.5 (see *O'Brien and Greenberg,* 2003). For example, *Pan and Sari* (2005) utilize a disruption criteria proportional to the gravitational binding energy of the body, and the equilibrium power law has q = 3. Numerical evolution simulations by *Kenyon and Bromley* (2004) and analytical work by *Pan and Sari* (2005) are in good agreement with the observation by *Bernstein et al.* (2004) of the number of bodies tens of kilometers in size. Note that the location of the break in size between the collisionally evolved and primordial populations increases with time and depends on the dynamical evolution of the system.

The size distribution of KBOs is likely to have a second break in slope at significantly smaller sizes. The second break corresponds to the transition between the collisionally evolved strength-dominated bodies and collisionally evolved gravity-dominated bodies. As the strength of KBOs is essentially unknown at present, the location of the strength to gravity transition based on catastrophic disruption models, e.g., tens to hundreds of meters (section 5.2), is highly uncertain.

In summary, the observed size distribution of KBOs departs from a single power law, which is consistent with the existence of both a collisionally evolved population and a primordial population (*Davis and Farinella,* 1997; *Kenyon and Bromley,* 2004; *Pan and Sari,* 2005; *Stern and Colwell,* 1997). In this scenario, the primordial populations should have experienced primarily surface modification processes through impact cratering events (section 3, Figs. 1 and 2a,b). The population of largest bodies probably has a subpopulation with differentiated internal structures (*Merk and Prialnik,* 2006) and a subpopulation with rubble-pile structures (*Davis and Farinella,* 1997). Both the collisionally evolved strength and gravity-dominated populations would have

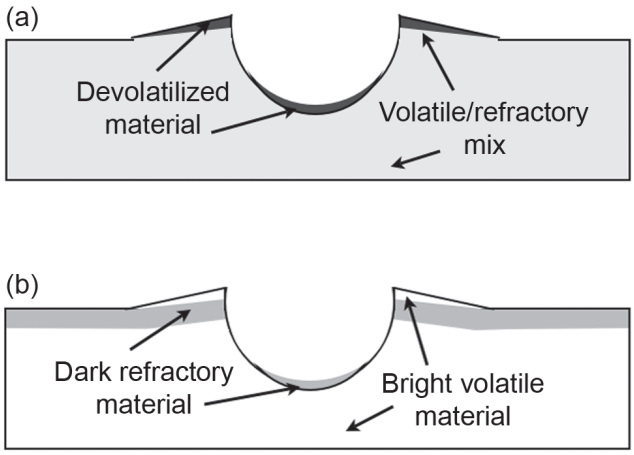

Fig. 1. **(a)** Schematic of an impact crater on a target made of a mixture of volatile and refractory material. The energy of the impact produces melting and devolatization at the base of the crater and in the ejecta. **(b)** Schematic of an impact crater on a target made mostly of volatile material. The surface of the target is covered with a "crust" of darker refractory material. The impact is large enough to excavate fresh volatiles from depth, creating a bright ejecta blanket. Collapse of the crater wall creates a darker region at the bottom of the crater.

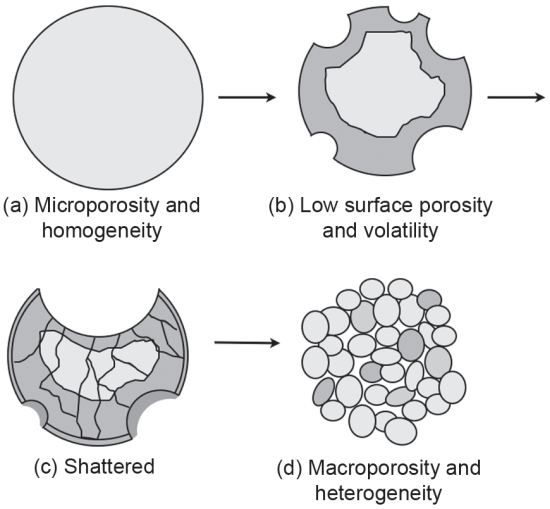

Fig. 2. Schematic showing a possible evolutionary track for a KBO. **(a)** A cross section through a primordial planetesimal with low bulk density and high microporosity. **(b)** After many small impacts, the bulk density has increased and volatile composition decreased at the surface. **(c)** After a large subcatastrophic collision, the body is shattered and the surface is covered with ejecta. **(d)** A catastrophic impact event disrupts the body, creating a rubble pile with high macroporosity and heterogeneous internal composition.

experienced the full range of collisional outcomes, including catastrophic disruption and changes in internal structure and composition (section 3, Fig. 2c).

2.3. Kuiper Belt Family (2003 EL_{61})

At present, a few tens of dynamical families have been identified in the asteroid belt (*Bendjoya and Zappalà,* 2002). These objects are grouped together in proper element space and have similar spectral features where detailed observations are available. The orbits of the family members can be integrated back in time to a common starting point, suggesting formation via a catastrophic collision. Although collisional evolution models of the Kuiper belt (section 2.2) indicate that very few KBOs larger than about 100 km have experienced catastrophic disruption events, *Brown et al.* (2007b) have observed what seems to be a collisional family in the Kuiper belt (see also chapter by Brown).

2003 EL_{61} has two known satellites and five proposed family members. All these objects have similar proper elements, colors, and a deep H_2O spectral feature (*Brown et al.,* 2007b). Although the detection of H_2O ice on the surfaces of KBOs is not unique to these objects, the significant depth of the spectral feature is characteristic of the proposed family, suggesting either more recent or more abundant exposure of surface ice compared to other KBOs. 2003 EL_{61} has a double-peaked rotational light curve with a period of 3.9 h (*Rabinowitz et al.,* 2006). Assuming that the lightcurve is solely due to the equilibrium shape of a rotating, homogeneous, fluid ellipsoid, *Rabinowitz et al.* (2006) and *Lacerda and Jewitt* (2007) derive the size (~1500 km diameter) and density (~2.6 g cm^{-3}). However, the derived size and density are highly uncertain as 2003 EL_{61} is likely to possess nonzero shear strength (*Holsapple,* 2007).

These combined observations suggest that 2003 EL_{61} suffered a significant but subcatastrophic impact event (*Brown et al.,* 2007b). If the modeled bulk density of 2.6 g cm^{-3} is correct and the precollision density of 2003 EL_{61} was comparable to other large KBOs (~2 g cm^{-3}; see chapter by Brown), then about 20% of the original mass was lost. In this model, the dispersed material was preferentially H_2O ice, presumably derived from an ice-rich mantle, producing the shared water spectral feature of the proposed family members.

Further investigation of the proposed 2003 EL_{61} family and search for other dynamical families would provide useful constraints on the collisional history of the Kuiper belt.

2.4. Total Mass of the Kuiper Belt

The total mass in the modern Kuiper belt is depleted from a smooth surface density extrapolation from the giant planet region of the solar system. Based on the observed size distribution of bodies between 30 and 50 AU, the total mass is only about 0.01 $M_\oplus$ (less than 5 $M_\mathbb{P}$) (*Bernstein et al.,* 2004). However, *Stern* (1996) and *Stern and Colwell* (1997) demonstrate that the Kuiper belt must have been more massive in the past for the largest KBOs (100 to 1000 km) to accrete via mutual collisions. At least 90% of the mass in the Kuiper belt was lost through collisions and ejections induced by the stirring and migrating of Neptune (*Stern and Colwell,* 1997; *Hahn and Malhotra,* 1999).

3. POSSIBLE COLLISION OUTCOMES IN THE KUIPER BELT

The observations summarized in the previous section indicate that collisions are an important factor in the evolution of the Kuiper belt. In studying the physical effects of collisions between KBOs, we are guided by the mature studies of collisions in the asteroid belt (*Asphaug et al.,* 2002; *Holsapple et al.,* 2002). However, the possible outcomes of collisions between KBOs are more diverse compared to asteroids because of the dynamical state of the system and the range of physical properties of individual KBOs. The important observations that inform the range of possible collision outcomes are as follows. The dynamical state of the Kuiper belt has changed dramatically with time (see chapter by Morbidelli et al.); hence the mutual collision velocities between KBOs also varied with time. In the modern Kuiper belt, the mutual collision velocities are around 1 km s^{-1} (*Trujillo et al.,* 2001) for classical KBOs and slightly higher for the other populations (see chapter by Gladman et al.). For these impact velocities, most bodies smaller than hundreds of kilometers in size have experienced a catastrophic disruption event, while most of the larger bodies have survived. All bodies should have suffered the production of a significant density of surface impact craters.

In addition to the dynamical impact conditions, the physical properties of KBOs are important. While the present observations are limited, the range of bulk densities of KBOs is <1 to ~2.6 g cm^{-3} (see chapter by Stansberry et al.) and the largest KBOs have a range of surface volatile compositions (H_2O, CH_4, etc.) in addition to a refractory (rock and organic) component (see chapter by Barucci et al.). From these observations and studies of short-period comets, believed to be fragments from KBOs, a typical KBO has a significant (but unknown) fraction of volatiles and high porosity.

Given the possible range of material properties and impact conditions, we outline the potential array of dramatically different outcomes from collisions between KBOs:

1. *Surface impact features.* As a result of the rich collisional history of the Kuiper belt, impact craters are expected to be common on the surfaces of KBOs. However, the morphologies and size distributions are sensitive to the surface and internal structure of the body. Some highly porous bodies survive the formation of multiple, large craters comparable to the radius of the object, as on the low-density asteroid Mathilde (*Veverka et al.,* 1997). Alternatively, only small craters may be observed on rubble piles formed by catastrophic disruption, such as asteroid Itokawa (*Fujiwara et al.,* 2006).

2. *Surface composition and color.* Impact craters and catastrophic disruption events may darken the surface by removing volatiles via heating from the energy of the im-

pact or brighten the surface of a body by excavating fresh ices (Fig. 1).

3. *Density of surface materials.* Laboratory impact craters in highly porous and compressible materials compact the impact site, creating density heterogeneity on the surface (*Housen et al.,* 1999). Over time, cumulative small impacts on a microporous surface may increase the bulk density and decrease the bulk porosity (Fig. 2a,b). In contrast, modeling results indicate that nearly all ejecta from a crater in a macroporous body may reach escape velocities, leaving the bulk density unchanged (*Asphaug et al.,* 1998).

4. *Internal structure and composition.* A subcatastrophic impact may shatter a body (and create a large crater) but leave the original internal material relationships intact (Fig. 2c), while a catastrophic impact both shatters and disperses a body such that the gravitationally reaccumulated remnants are rubble piles with high macroporosity and mixed composition (Fig. 2d).

In the next section, we describe the factors that control the outcome from individual collision events.

4. FACTORS THAT CONTROL OUTCOMES OF COLLISIONS

Recent advances in the understanding of the physics of collisional processes between icy, porous bodies provide new fuel to the study of the role of collisions in the Kuiper belt. The outcome of collision events are governed by the impact conditions (velocity, angle, and mass of each body) and the physical properties of the colliding bodies (strength, composition, and internal structure). Both the impact conditions and physical properties affect the efficiency with which the energy of the impact is coupled to the target. In this section, we summarize four overarching factors that control the outcome of an impact event between KBOs. In the following section (section 5), we will describe laboratory and numerical experiments on KBO analog materials that investigate these controlling factors.

First, the composition and internal structure of the bodies determines the critical velocity required to enter the strong shock regime, where the deformation and coupling of energy and momentum can be described through the Rankine-Hugoniot conservations equations (section 4.1). Slower impact events, where plastic deformation dominates, require more detailed knowledge of the physical properties (particularly strength) of the bodies compared to the strong shock regime. Collisions between KBOs are likely to span the range of plastic and shock deformation.

Second, the final outcome is a balance between the forces of strength and gravity (section 4.2). Scaling laws have been developed for cratering and catastrophic disruption in each regime, but a large transition region exists. Because of the low gravity and expected low strength of KBOs, many collisions may fall in the transition region.

Third, the internal structure and composition of the colliding bodies may significantly affect collision outcomes (section 4.3). Some of the impact energy will be partitioned into phase changes when highly volatile materials are present. High levels of porosity also alter the energy coupling by acting as a shock absorber and localizing shock deformation. The momentum coupling with high porosity changes the excavation flow in the cratering regime and the dispersal of fragments in the disruption regime compared to collisions between solid bodies.

Fourth, collision outcomes are sensitive to the mass ratio of the projectile and target. At the same kinetic energy, a larger projectile is more efficient at removing mass than a smaller projectile (section 4.4).

4.1. Shock Deformation

In most high-energy impact events, the deformation is driven by a shock wave. The energy from the shock controls the physical deformation from the collision, such as fragmentation, pore collapse, heating, and phase changes. The shock also determines the deposition of momentum that leads to crater excavation or dispersal of fragments following a catastrophic disruption event. The amount of deformation can be estimated by considering the volume of material shocked to a given peak pressure.

A strong shock wave is produced in a *hypervelocity* impact event, where the impact velocity exceeds the bulk sound speed (c_b) in both the target and projectile. However, mutual collision velocities between KBOs are likely to span the range from subsonic to supersonic (hypervelocity) collisions (see below). When collisions are comparable to the sound speed, plastic deformation dominates, rather than strong shock deformation. Under subsonic conditions, collisions are simply elastic and governed by the coefficient of restitution.

In this section, we present a summary of the shock physics that determines the outcome in the hypervelocity regime. The peak shock pressure is deduced from the conservation equations and material equation of state, describing the pressure-volume-temperature (P–V–T) states. A shock wave satisfies the Rankine-Hugoniot (R-H) mass, momentum, and energy conservation equations (*Rice,* 1958)

$$u_i - u_0 = U_S\left(1 - \frac{V_i}{V_0}\right) \quad (1)$$

$$P_i - P_0 = \left(\frac{U_S}{V_0}\right)(u_i - u_0) \quad (2)$$

$$E_i - E_0 = \frac{1}{2}(P_i - P_0)(V_0 - V_i) \quad (3)$$

In the above formulae u is particle velocity, U_S is shock velocity, V is specific volume (= $1/\rho$, where ρ is density), P is pressure, and E is specific internal energy. The initial unshocked state is subscripted $_0$ and the final shocked state is subscripted $_i$.

The shock Hugoniot is the curve that describes the locus of possible P–V shock states for a given initial P–V–T state.

For a given impact scenario, the shock pressure is calculated using equation (2), the impact velocity, and the equations of state of the target and projectile. Many materials may be described using a simple linear U_S–u shock equation of state of the form (*Ruoff,* 1967)

$$U_S = c + su \quad (4)$$

where c and s are material constants (for their relationship to finite strain theory, see *Jeanloz,* 1989). The linear shock equation of state is simply a representation of the P–V shock Hugoniot translated into U_S–u space using the R-H equations.

In the planar impact approximation (also called the impedance match solution; see derivation in *Melosh,* 1989), the particle velocities induced by the shock wave reduces the projectile's velocity and mobilizes the target such that continuity at the projectile-target interface is achieved and

$$u_t = v - u_p \quad (5)$$

where v is the impact velocity and subscripts $_t$ and $_p$ refer to the target and projectile, respectively. The shock pressure is derived by solving for u_t using the equality of equation (2) in the target and projectile and substituting equations (4) and (5)

$$\rho_{0,t}(c_t + s_t u_t)u_t = \rho_{0,p}(c_p + s_p(v - u_t))(v - u_t) \quad (6)$$

The quadratic function for u_t is readily solved. In the case of identical shock equations of state in the target and projectile, the particle velocity is equal to v/2, and the peak pressure is given by $\rho_0(c + sv/2)(v/2)$. Because of strength and phase changes, the U_S–u shock equations of state for natural materials are usually fit with multiple linear segments in u, corresponding to different pressure ranges on the shock Hugoniot. The shock equations of state for many rocks and minerals are compiled in *Ahrens and Johnson* (1995a,b), and the equations for nonporous and porous H_2O ice are given in *Stewart and Ahrens* (2004, 2005).

As the shock wave propagates into the target, the peak pressure, derived from the planar impact approximation, decays from rarefaction waves on the free surfaces. The size of the region at peak pressure (known as the isobaric core) and the decay exponent depend on the impact velocity and material properties (e.g., equation of state and porosity) (*Ahrens and O'Keefe,* 1987; *Pierazzo et al.,* 1997). In general, the pressure decay is steeper for high velocities because of energy partitioning into phase changes. The occurrence of impact-induced phase changes can be estimated by considering the critical shock pressures required for melting and vaporization. When the shock pressure is above a critical value, the material is melted/vaporized after passage of the shock wave and return to ambient pressure conditions.

The present mean mutual collision velocity between classical KBOs (~1 km s^{-1}) is lower than the bulk sound speed of full density silicates and ices. Nonporous H_2O ice has a c_b of 3.0 km s^{-1} at 100 K (*Petrenko and Whitworth,* 1999; *Stewart and Ahrens,* 2005). Silicate rocks have larger c_b, typically around 5 km s^{-1} (*Poirier,* 2000). Sound speeds of laboratory preparations of nonporous ice-silicate mixtures, with up to 30 wt% sand, are similar to pure H_2O ice (*Lange and Ahrens,* 1983). Pure porous H_2O ice, on the other hand, can have much lower sound speeds, from 0.1 to 1.0 km s^{-1} for bulk densities of 0.2 to 0.5 g cm^{-3} (*Mellor,* 1975; *Furnish and Remo,* 1997). Silica aerogels with densities of about 0.2 g cm^{-3} have sound speeds of about 200 m s^{-1} (*Gross et al.,* 1988), and 35% porous sand has a sound speed of 130 m s^{-1}. If KBOs are volatile rich and porous, then mean present-day collisions may be supersonic.

During the collisional evolution of the Kuiper belt, collisions span the subsonic to supersonic regimes. Understanding the controlling physics in the subsonic regime, where plastic deformation dominates, will require focused studies on analogs for the range of mechanical structures in the Kuiper belt (section 5). In the strong shock regime, crater scaling relationships and catastrophic disruption theory are applicable, as described in the next section.

4.2. Strength and Gravity

The final outcome of a collision, e.g., crater size or dispersed mass, depends on the balance between strength and gravitational forces. In the case of impact cratering, the relationship between the size and velocity distribution of the impacting population and the observed crater population can provide insight into the collisional history of a system [as has been done for the terrestrial planets (*Strom et al.,* 2005) and asteroids (*O'Brien and Greenberg,* 2005)]. Backing out the impactor properties requires the application of the appropriate crater scaling relationships, which depend on both the impact conditions and material properties. In the case of catastrophic disruption, knowledge of the properties of the populations of disrupted and primordial bodies provide strong constraints on the collisional evolution of the Kuiper belt. Here, we present the crater size and catastrophic disruption scaling laws in the strength and gravity regimes.

4.2.1. Crater scaling theory. Development and validation of the appropriate scaling relationships is crucial for the next generation of collisional evolution models of KBOs that include consideration of physical deformation effects. Because of their low gravity and likely low strength, the outcome of collisions between KBOs is near the transition between the strength and gravity regimes. In this section, we discuss the strength to gravity transition and summarize the equations and material parameters for crater scaling for comparison to laboratory craters in ice and porous targets in section 5.1.

In a cratering event, the shock-driven excavation flow produces a roughly hemispherical cavity, called the transient crater. Assuming that material strength can be represented by a single parameter, Y, the transition size between the strength and gravity-controlled cratering regimes is pro-

portional to Y/ρg. Y is the dominant strength measure that controls crater size (e.g., shear strength); ρ is the bulk density of the target; and g is the gravity of the target (*Melosh,* 1977; *Melosh and McKinnon,* 1978). As the impact energy increases, the outcome of collisions will transition from a cratering regime to a total body disruption regime. The criteria for catastrophic disruption, Q_D^*, is defined as the specific energy (kinetic energy of the projectile divided by the mass of the target) required to disrupt and gravitationally disperse half the mass of the target (*Melosh and Ryan,* 1997). Note that, unlike the cratering regime, disruption is governed by the bulk tensile strength of the body, which is typically an order of magnitude lower than the compressive strength of brittle solids (see sections 4.2.2 and 4.4).

The theory for crater size scaling based on impact parameters and material properties is summarized by *Holsapple* (1993). A common approach utilizes π-scaling, with empirical constants derived from impact and explosion cratering experiments under Earth's gravity and high gravity. Predicting the final crater volume and shape requires two steps: (1) calculating the volume of the transient crater cavity using the π-scaling laws and (2) calculating the amount of collapse of the transient crater to the final crater volume and shape. The first step is better understood than the second.

In π-scaling, the cratering efficiency, π_V, is defined as the ratio of the mass of material ejected and displaced from the transient crater cavity to the mass of the projectile

$$\pi_V = \frac{\rho V}{m_p} = \frac{M_c}{m_p} \tag{7}$$

where V is the volume of displaced and ejected material, m_p is the mass of the projectile, and $M_c = \rho V$. For strength-dominated craters, the cratering efficiency depends on the ratio of a measure of the shear strength of the target, $\bar{Y}$, to the initial dynamic pressure, given by

$$\pi_{\bar{Y}} = \frac{\bar{Y}}{\rho v_\perp^2} \tag{8}$$

where, $v_\perp = v \sin\theta$, v is the impact velocity, and θ is the impact angle from the horizontal. In the gravity-dominated regime, the cratering efficiency depends on the ratio of the lithostatic pressure at a characteristic depth of one projectile radii, r_p, to the normal component of the initial dynamic pressure (the inverse Froude number)

$$\pi_2 = \frac{g r_p}{v_\perp^2} \tag{9}$$

where g is the gravitational acceleration.

Impact experiments demonstrate that the transition from strength- to gravity-dominated cratering spans about two decades in π_2. Following *Holsapple* (1993) and *Holsapple and Housen* (2004), the cratering efficiency can be defined by an empirical, smoothed function of the form

$$\pi_V = K\left(\pi_2 + \pi_{\bar{Y}}^{\beta/\alpha}\right)^{-\alpha} \tag{10}$$

where the exponents are related to a single coupling exponent, μ, by $\alpha = 3\mu/(2 + \mu)$ and $\beta = 3\mu/2$. The coupling exponent μ is bounded by two cratering regimes: momentum scaling (where $\mu = 1/3$) and energy scaling ($\mu = 2/3$) (*Holsapple and Schmidt,* 1987; *Holsapple,* 1987). Note that equation (10) assumes that the target and projectile have the same density. The transition from strength to gravity dominated regimes occurs when $\bar{Y} \sim \rho g r_p$.

In Plate 3, cratering efficiencies are presented for liquid water (K = 0.98, μ = 0.55, $\bar{Y}$ = 0 MPa), dry sand (K = 0.132, μ = 0.41, $\bar{Y}$ = 0 MPa, 35% porosity) and weak rocks (K = 0.095, μ = 0.55, $\bar{Y}$ = 3 MPa) (values from *Holsapple and Housen,* 2004). Dry sand is a noncrushable porous material and weak rock is a reasonable analog for nonporous H_2O ice. Cratering efficiencies in crushable, porous materials, from hypervelocity experiments in vacuum, lay a factor of a few below the dry sand line (*Schultz et al.,* 2005). The transition from strength regime (lower values of π_2, when $\pi_{\bar{Y}} > \pi_2$) to gravity regime (higher values of π_2) corresponds to the transition from a horizontal line in a π_V–π_2 plot, when the cratering efficiency is independent of π_2, to a power law with slope –α. The cratering efficiency in the strength regime increases with increasing impact velocities, as indicated by the curves for impacts into weak rock targets at 0.5, 2.0, and 7.0 km s^{-1}. Note that the cratering efficiency in dry sand is less than for weak rock in the gravity regime because of energy dissipation in the porous sand. Data from impact cratering experiments conducted in vacuum under Earth's gravity into nonporous ice (▲; *Cintala et al.,* 1985; *Lange and Ahrens,* 1987; *Burchell and Johnson,* 2005) and 50% porous ice (●; *Koschny et al.,* 2001; *Burchell et al.,* 2002) fall in the strength regime. Cratering experiments at 1.86 km s^{-1} in porous mixtures of sand and perlite bonded with fly ash and water under 1 atm of pressure and varying gravity are nearly independent of π_2, indicating strength-dominated behavior with a plausible intersection with the gravity-dominated regime (the dry sand line) (section 5.1.3) (*Housen and Holsapple,* 2003).

Cratering events in the Kuiper belt by a nominal 0.5-m radius body at 1 km s^{-1} onto targets of 0.1–1000-km radii correspond to π_2 values in the range from 10^{-10} to 10^{-6}. Therefore, for the range of impact velocities in the Kuiper belt, Plate 3 demonstrates that the presence of any strength is likely to control the final crater size for the majority of impact events. In the upper range of possible values of π_2, gravity may dominate if cratering is less efficient in KBOs than in dry sand.

After formation of the transient crater cavity by the excavation flow, most craters undergo collapse to a final crater shape (*Melosh and Ivanov,* 1999). For simple, strength-dominated craters, the final crater size is similar to the

transient cavity with some collapse of the crater walls. For cratering in soils and rocks, the rim radius of the transient crater is approximately $R_r = 1.73V^{1/3}$ (*Holsapple,* 1993). Complex, gravity-dominated craters undergo significant collapse of the transient cavity, and the final crater rim radius scales with the transient crater rim radius and gravity by $R_{complex}(cm) = 0.37R_r(cm)^{1.086}(g/g_{Earth})^{0.086}$ (*Holsapple,* 1993).

The final state of crater formation in porous, icy bodies is not well understood. In section 5, we discuss some of the laboratory experiments that provide our best guesses at the appropriate crater size scaling laws for the Kuiper belt.

4.2.2. Catastrophic disruption theory. Based on the models of the collisional evolution of the Kuiper belt, it is probable that a large fraction of bodies have suffered both cratering events and disruptive collisions. The catastrophic disruption criteria, Q^*_D, is the ratio of the projectile's kinetic energy to the mass of the target required to disrupt and disperse half the mass of the target.

The criteria has two components (*Davis et al.,* 1979)

$$Q^*_D = Q^*_S + Q_b \qquad (11)$$

where Q^*_S is the strength of the body to shattering and Q_b is the gravitational binding energy of the target.

The catastrophic disruption criteria for a rocky body is shown by the thick solid line in Fig. 3 (section 5.2.2) (*Benz and Asphaug,* 1999). The critical energy is averaged over all impact angles. A head-on collision is most efficient, requiring about an order of magnitude less energy compared to the angle average (*Benz and Asphaug,* 1999; *Leinhardt et al.,* 2000; *Leinhardt and Richardson,* 2002). In the strength regime, where Q^*_S dominates, the critical energy decreases with increasing target size because tensile strength, the controlling strength measure, is scale dependent (*Housen and Holsapple,* 1999). The larger the body, the larger the number of preexisting natural flaws and the lower the tensile strength. In the gravity regime, pressure from the self-gravity of the object increases the strength, following the shattered rock curve for head-on impacts (*Melosh and Ryan,* 1997). In the gravity regime, the gravitational dispersal criteria dominates over shattering by orders of magnitude. Note that the standard disruption criteria curves assume that the size of the projectile is small compared to the target (see section 4.4).

The manner in which volatile content and porosity affect the disruption criteria is not well understood. Here, we estimate the effects of each using nonporous and porous H_2O ice as an example. There has been little work on catastrophic disruption of large objects in the gravity regime at impact speeds and compositions that are relevant to the the present day Kuiper belt, thus this discussion is meant to provide general guidance, not detailed values.

In the strength regime, the Q^*_D intercepts for nonporous and porous ice (thin solid line and dashed line, respectively) are tied to results from laboratory disruption experiments (see section 5.2.1) (*Arakawa et al.,* 2002). These values are consistent with other experimental results (*Ryan et al.,* 1999). The slope of Q^*_S for pure ice is assumed to be the same as for rock. For porous ice, on the other hand, the slope in the strength regime is particularly uncertain. The slope for porous materials may be much shallower than for nonporous materials because the size-dependent scaling of flaws may not apply (*Housen and Holsapple,* 1999). This uncertainty is depicted in Fig. 3 by several dashed lines of varying slope. Perhaps counterintuitively, in the strength regime, a porous material is harder to disrupt than a nonporous material due to localization of energy by compaction of pores and/or reflection of the shock wave off of free surfaces (see section 5.2.1).

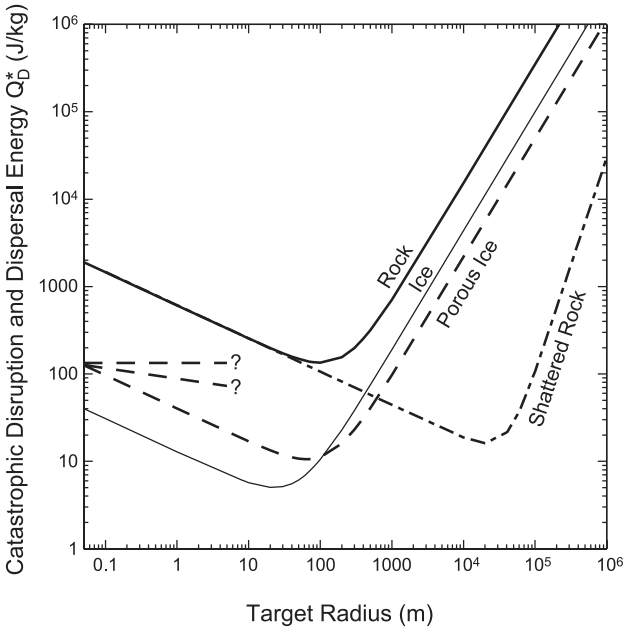

Fig. 3. Catastrophic disruption and dispersal energy (Q^*_D) vs. target radius for rock (thick solid line), nonporous ice (thin solid line), 50% porous ice (dashed line). The negatively sloped portions of the curves are in the strength regime, the positive slopes are in the gravity regime. The criteria for rock is based on angle averaged results from 3 km s^{-1} collisions onto basalt (*Benz and Asphaug,* 1999). The nonporous and porous ice intercepts are based on laboratory experiments (*Arakawa et al.,* 2002) (Q^*_D = 40 J kg^{-1} and Q^*_D = 143 J kg^{-1} for low- and high-porosity targets, respectively, of 5-cm radius). The extrapolation into the gravity regime is highly uncertain for porous materials. These results assume energy coupling by a small projectiles compared to the size of the target.

In the gravity regime, the Q^*_D criteria for nonporous ice lies below the rock criteria by the ratio in mass (for this plot vs. target size). This is consistent with the numerical impact simulations into ice targets by *Benz and Asphaug* (1999). Similarly, a porous target of the same size is easier to disrupt because of its lower total mass. Adjusting the gravity-dominated Q^*_D criteria by the ratio in total mass makes the unreliable assumption that the energy coupling from the collision is similar for each material. Because of the significant dissipative effects of porosity, porosity may have a large affect on energy coupling in the gravity regime (the

Q_S^* term may be more significant). More work is needed to determine exactly how porosity affects the energy coupling for catastrophic disruption events.

As with impact cratering events, it is clear that in order to predict the collision outcome from a disruption event, it is necessary to know something about the material properties of the KBOs. In the case of catastrophic disruption, global properties, rather than surface properties, are more important; e.g., is the target porous, icy, rocky? In section 5.2, we discuss the small amount of work on catastrophic disruption of KBO analog materials.

4.3. Internal Structure and Composition

Kuiper belt objects are likely to possess a wide variety of internal structures, as depicted in Fig. 2. Dynamical excitation and increased collision frequencies from the migration of Neptune removed most of the mass from the original Kuiper belt, leaving a mixture of collision fragments and unmodified material (*Davis and Farinella,* 1997; *Hahn and Malhotra,* 1999; chapter by Morbidelli et al.). Comets may provide clues to the present internal structure of KBOs; however, comets are expected to be diverse themselves (chapter by Barucci et al.; *Weissman et al.,* 2005).

Porosity, either primordial or the result of collision events, is a major complicating factor in predicting the amount of shock deformation. Since KBOs are expected to contain a range of porosities, the outcome of individual collisions could vary widely depending on the properties of the colliding bodies. When the initial porosity is high, the shock impedance (the bulk density times the sound speed) is low, and the peak shock pressures produced for a given impact condition are lower compared to a solid target (equations (1) and (2)). For a given shock pressure, however, the internal energy increase is larger in a porous material because of the greater change in volume during shock compaction (equation (3)). Hence, the temperature rise due to a shock is higher in porous materials, and impacts into porous ices may result in abundant melting or vaporization near the impact site (*Stewart and Ahrens,* 2004, 2005). Porosity is an efficient dissipator of shock energy. As the shock propagates into the target, porosity increases the decay rate of the shock because of the increased energy partitioning into heat (e.g., *Meyers,* 2001). Therefore, the shock-deformed volume in porous materials is smaller compared to a solid.

The length scale of the porosity is also important. Small-scale porosity compared to the shock thickness is described as *microporosity*. The thickness of the shock wave is proportional to the scale of the topography on the surface of the projectile. Large-scale porosity, e.g., a rubble pile of solid pieces, is described as *macroporosity*. In the latter case, the solid (e.g., monolithic) pieces may have high strength, and impact cratering events onto a monolithic piece would reflect the high surface strength. For catastrophic disruption events, however, a rubble pile has low bulk tensile strength. In a rubble pile, the shock wave would reflect upon encountering void space between solid boulders, and as a result, the energy from the shock would be deposited in a smaller volume compared to a shock wave propagating through a monolith of competent rock. On the other hand, a microporous body may have low surface compressive strength, but because of the efficient shock dissipation, a more energetic impact is required to catastrophically disrupt the body (*Asphaug et al.,* 1998). Hence, both macroporous and microporous bodies may have high *disruption strength*.

Compositional variation and surface layers also change the way energy is coupled into the target. The impact energy will be partitioned into more compressible phases and a larger Q_D^* is required to disrupt a more compressible material (*Benz and Asphaug,* 1999). Because some of the energy of the impact is partitioned into heating, each collision event will also result in net devolatilization. Finally, phase changes (melting, vaporization) of volatile materials will result in steeper decay of the shock wave (*Ahrens and O'Keefe,* 1977; *Pierazzo et al.,* 1997; *Pierazzo and Melosh,* 2000) that tends to localize the shock deformation in a manner similar to the effects of porosity.

4.4. Mass Ratio

The mass ratio of the colliding bodies is also an important factor in determining the collision outcome. In simulations of subsonic collisions, *Leinhardt and Richardson* (2002) found that smaller projectiles were not as efficient at disrupting targets as larger projectiles (see Fig. 4) (*Leinhardt and Richardson,* 2002; *Melosh and Ryan,* 1997). The mass ratio affects the volume over which the impact energy and momentum are deposited. When the projectile is much smaller than the target, the impact directly affects a small volume, about the size of the projectile. The rest of the target acts to dampen any material motion. When the projectile mass is similar to the target mass, on the other hand, the projectile comes in direct contact with a significant volume fraction of the target. As a result, the specific energy required to catastrophically disrupt a target decreases by orders of magnitude.

The dependence on mass ratio has not been studied directly for hypervelocity impacts, although the dependence on the coupling of energy and momentum should be similar to the subsonic case. First, the size of the peak pressure region (isobaric core) is proportional to the size of the projectile. Second, the decay of the peak shock pressure with distance depends on the impact velocity. The decay is steeper for higher-impact velocities because more energy is partitioned into phase changes and deformation. Low-impact velocities have a more shallow decay exponent (in the elastic limit). The particle velocities are proportional to the peak shock pressure; thus the shock pressure profile in the target will affect the dispersal of fragments and the catastrophic disruption criteria. Q_D^* should decrease as the projectile size increases for a fixed kinetic energy of the projectile.

Let us now consider a likely impact scenario in the Kuiper belt. For an example 100-km volatile-rich target in

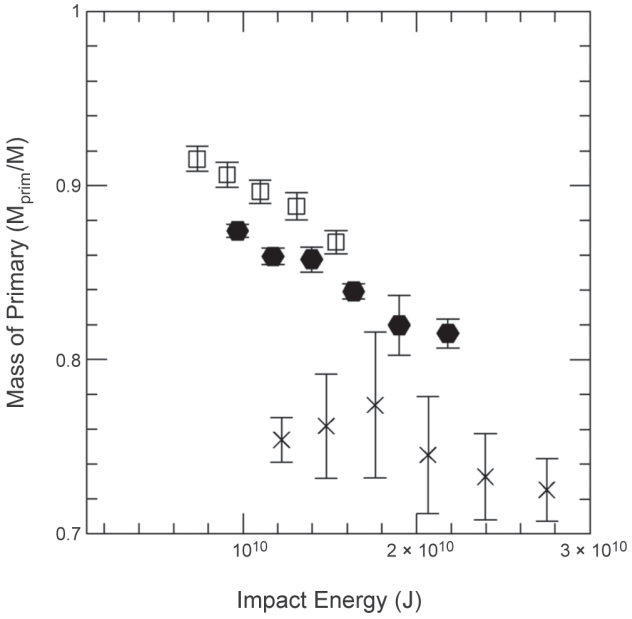

Fig. 4. Mass of the largest reaccumulated body (M_{prim} in units of total system mass $m = M_{proj} + M_{targ}$) following a large collision event as a function of the kinetic energy of the projectile. Results from N-body impact simulations of km-sized rubble piles in the subsonic regime (*Leinhardt and Richardson,* 2002). The crosses, filled hexagons, and open squares denote projectile to target mass ratios of 1:3, 1:6, and 1:9, respectively. In all cases, targets were identical with a radius of 1 km. All data points are averaged over several simulations at various impact angles (rms error bars). Note that, for the same kinetic energy, the largest projectiles produced the smallest largest post-collision remnant. These results indicate that increasing the projectile size increases the disruption efficiency.

the Kuiper belt, Fig. 3 predicts that about 10^5 J kg^{-1} is necessary for catastrophic disruption. At 1 km s^{-1}, the projectile would have a radius two-thirds that of the target. However, Fig. 3 assumes small (point source) projectiles. As the projectile to target mass ratio approaches unity, the amount of energy per target mass needed to disrupt the target drops (*Holsapple,* 1993; *Melosh and Ryan,* 1997; *Leinhardt and Richardson,* 2002). Therefore, a 100-km target may indeed be catastrophically disrupted by a smaller projectile than predicted in Fig. 3, and the larger objects in the Kuiper belt may have suffered more catastrophic or near-catastrophic impacts than inferred in previous studies. More work is needed to determine how Q_D^* behaves with mass ratio in hypervelocity collisions.

5. STUDIES OF COLLISIONS IN ANALOGS TO KUIPER BELT OBJECTS

We now turn to laboratory and numerical experiments on the major factors that affect the collision outcomes described above. Laboratory experiments and numerical models of collisions between icy and/or porous bodies serve as the best analogs at present for impacts into KBOs. There is a large body of laboratory work on cratering impacts into volatile ices and mixtures as well as porous material (section 5.1). Although a coherent theory will require additional experiments, the laboratory results are a good guide to the possible outcomes of cratering collisions on KBOs. In comparison, the laboratory and numerical experiments on catastrophic disruption of KBO analogs are more limited (section 5.2). This is due in part to the inability to study catastrophic disruption in the gravity regime in the laboratory and the difficulties in modeling collisions between porous, volatile bodies.

5.1. Cratering

We begin with the results of several impact cratering studies into nonporous H_2O ice and ice-silicate mixtures (section 5.1.1). Then, the effects of porosity are introduced (section 5.1.2). However, it is difficult to deconvolve the effects of porosity and low material strength in laboratory studies. Possible outcomes include cratering events that result in compaction rather than the normal crater excavation flow (section 5.1.3). Relatively little work has been conducted on ices more volatile than H_2O, which have been observed on the surfaces of the largest KBOs (see chapters by Barucci et al. and Brown) (section 5.1.4). Finally, experiments into targets with surface layers of different strength materials can also have a significant affect on the crater morphology (section 5.1.5). Because of the influence of an atmosphere on the final crater form, explosion cratering studies (*Holsapple and Housen,* 2004) are not included in this discussion.

5.1.1. Cratering in nonporous H_2O ice and ice-silicate mixtures. As a low-density and volatile material, solid H_2O ice represents a very simple model for the bulk properties of KBOs. Depending on the evolution of KBOs, some surfaces may be dominated by solid ice. Most laboratory impact experiments in ice are conducted in the strength regime. Generally, cratering efficiencies in solid ice are similar to a dry soil or weak rock (Plate 3) (*Chapman and McKinnon,* 1986). Solid ice cratering experiments span impact velocities of 0.1–7.3 km s^{-1} using a wide range of projectile materials (*Burchell and Johnson,* 2005; *Croft et al.,* 1979; *Lange and Ahrens,* 1982, 1987; *Shrine et al.,* 2002; *Grey and Burchell,* 2003; *Kawakami et al.,* 1983; *Kato et al.,* 1995; *Iijima et al.,* 1995; *Cintala et al.,* 1985). For a given impact energy, the crater volume is more than an order of magnitude larger than craters formed in a typical hard silicate rock. In many of these experiments, the measured volumes of the craters include a component of spalled material (near-surface material ejected under tensile failure), forming a terraced crater morphology with a central pit. Hence, the reported volumes are larger than the transient crater volume and comparisons to π-scaling laws must be made with caution. Also, differences in ice target preparation contribute to scatter between experiments.

Impact cratering experiments in solid H_2O ice have investigated the effects of target temperature on the cratering efficiency (*Lange and Ahrens,* 1982, 1987; *Grey and Burchell,* 2003). Low-temperature ice has a cratering efficiency

between temperate ice and hard rock. Under fixed impact conditions, the crater depth and volume decreased by factors of 2 and 4, respectively, as the ice temperature decreased from 253 K to 100 K (*Grey and Burchell,* 2003). It is well established that the yield strength of ice increases as the temperature decreases (e.g., *Sammonds et al.,* 1998); however, the magnitude of the effect is not well predicted (*Grey and Burchell,* 2003).

Thermodynamic analyses of shock wave experiments on solid H_2O ice at 100 K indicate that peak shock pressures of 1.6 and 4.1 GPa are required to produce incipient and complete shock-induced melting, respectively (*Stewart and Ahrens,* 2005). For pure ice on ice impacts, these pressures are achieved at impact velocities of about 1 and 2 km s^{-1}. If the bulk shock impedance of solid ice is similar to porous volatile-refractory mixtures, mass melting of solid ice within KBOs is only expected at the upper end of the range of collision velocities within the Kuiper belt (0.5–3 km s^{-1}) (*Dell'Oro et al.,* 2001).

Nonporous mixtures of ice and silicates (e.g., ice-saturated sand) have also been studied in the strength regime (*Croft et al.,* 1979; *Koschny and Grün,* 2001). The cratering efficiency decreases with increasing silicate content.

5.1.2. Cratering in porous material. Several groups have conducted cratering experiments into porous materials (*Schultz et al.,* 2005; *Schultz and Gault,* 1985; *Schmidt,* 1980; *Housen et al.,* 1999; *Housen and Holsapple,* 2003; *Koschny et al.,* 2001). The porous targets include porous ice, sand, Ottawa flint shot, pumice, and vermiculite. Hypervelocity impact experiments, conducted under vacuum, into pumice powder with porosities between 35% and 50% follow a single gravity-controlled crater scaling that is slightly less efficient than dry sand (Plate 3) (*Schultz et al.,* 2005). However, for lower-velocity impacts, in the strength regime or in the transition between strength and gravity-dominated cratering, the effects of porosity can be significant (section 5.1.3).

Results from cratering experiments into ~50% porous (*Koschny et al.,* 2001; *Burchell et al.,* 2002) and solid ice targets indicate that the displaced and ejected mass scales linearly with impact energy. In other words, the crater volume is proportionally larger by the difference in target density. However, it is unlikely that this result can be extrapolated to events with much larger impact energies because of the considerable effects of vaporization on the final crater size (*Holsapple and Housen,* 2007; *Schultz et al.,* 2005).

Because of the large increase in internal energy associated with shock compaction of porous H_2O ice, the critical pressures required for shock-induced melting are lower compared to solid ice. From shock wave experiments, *Stewart and Ahrens* (2004) find that shock pressures of only 0.3 to 0.5 GPa initiate melting in 40–45% porous ice, and complete melting is reached by 2 GPa. These pressures correspond to impact velocities in the range of 1–2.5 km s^{-1} for collisions between porous ice bodies. Although porous ice has lower shock impedance than solid ice, the increase in internal energy from pore compaction results in similar critical impact velocities for shock-induced melting. If KBOs have shock impedances greater than pure porous H_2O ice, as expected if they are ice-refractory mixtures, then mutual collisions under the present dynamical environment will result in abundant melting of H_2O ice.

Therefore, shock-induced melting in porous targets may produce crater cavities lined with quenched melt (rapidly cooled liquid that solidifies as a glass). Quenched melt lined craters have been observed in laboratory impact experiments into 50% porous H_2O ice (nylon projectiles at 0.9–3.8 km s^{-1}) (*Koschny et al.,* 2001) and 5–60% porous soda lime glass (glass projectiles at 4.9–6.1 km s^{-1}) (*Love et al.,* 1993). In some cases, all the impact-generated melt was ejected from the crater. Hence, cratering events onto porous KBOs may produce solid ice ejecta fragments.

The depth of penetration of the projectile plays a significant role in the cratering efficiency in porous materials. In hypervelocity impacts, the impact angle determines the outcome. For example, the cratering efficiency in compressible porous perlite granules (ρ = 0.2 g cm^{-3}) increases as the impact angle decreases from 90° to 30° (*Schultz et al.,* 2005). Vertical impacts into porous materials penetrate deeply into the target, resembling a deeply buried explosion. Low-angle impacts, in contrast, reach a more optimal shallow depth of burial to produce a larger crater. In the low-velocity regime, an impedance mismatch between the target and projectile will also influence the depth of penetration. A dense projectile may experience little deformation and penetrate deeply, resulting in less-efficient cratering compared to a projectile with density that matches the target. Interpretation of the cratering record on KBOs will need to include the role of impact angle and the depth of penetration in the final crater size.

In the case where the projectile is more dense than the target (e.g., a solid rock meteoroid impacting a porous KBO), the impact conditions may be supersonic for the target but subsonic for the projectile. In this case, the projectile is not significantly disrupted by the impact event. Laboratory experiments show that the penetration depth increases as the density contrast between the projectile and target increases (*Love et al.,* 1993). Intact or melted nylon (ρ = 1.14 g cm^{-3}) and copper (ρ = 8.92 g cm^{-3}) projectiles were recovered after impacts at velocities up to 7 km s^{-1} into 50% porous H_2O ice (*Koschny et al.,* 2001; *Burchell et al.,* 2002). The experimental results suggest that dense meteoroids may embed themselves into the surfaces of KBOs and comets. In a pathological example, a population of compacted, devolatilized projectiles might be found embedded in the surfaces of very porous, volatile KBOs.

Reliable numerical models of crater formation in porous materials have been hindered by the difficulty in modeling the shock compaction of porous materials (e.g., *Herrmann,* 1969; *Johnson,* 1991). Some general results can be drawn from the relatively few simulations to date: (1) a proxy model for porosity using layers of solid ice and void and the Autodyne code (*Burchell and Johnson,* 2005), (2) a P-alpha crush-up model for sand using the CTH code (*Housen and Holsapple,* 2000), and (3) a new ε-alpha compaction model using the iSALE code (*Wünnemann et al.,* 2006).

In summary, the transient crater diameters in porous materials are smaller but the crater is deeper than those in nonporous media. The lower bulk density of the porous target allows the projectile to penetrate more deeply. The shock wave is attenuated more quickly in porous material because energy is partitioned into crushing pores. These numerical experiments show that porous crushable objects are more resilient to large impact than nonporous objects because the damage from the impact is much more localized. With these more advanced models of porosity, future work can address the volume of material that experiences deformation (fragmentation, devolatilization) from impact events in the Kuiper belt.

5.1.3. Compaction cratering. Observations of an unusual main-belt asteroid, 253 Mathilde, have incited several studies on the role of porosity on impact cratering. Imaged during a flyby of the NEAR spacecraft, Mathilde has a low bulk density (~1.3 g cm^{-3}) and exhibits four large impact craters with diameters larger than the mean diameter of the asteroid (*Veverka et al.,* 1997). The large craters have no visible ejecta blankets or raised rims. As a result of their size, the craters are very close to each other and yet seem to show no evidence of interaction. The unique characteristics of Mathilde suggest that the internal structure of this C-type asteroid is different from other classes of main-belt asteroids in a fundamental way.

Housen et al. (1999) and *Housen and Holsapple* (2003) conducted a series of cratering experiments into compressible, porous material in an attempt to explain the craters on asteroid 253 Mathilde. The authors suggest that high microporosity (40–60%) and high compressibility lead to a phenomena they termed compaction cratering.

In their studies, the projectile and impact velocity was held constant, and the target porosity and gravity (using a centrifuge) were varied. In the high-gravity environment, the craters had no raised rims and minimal ejecta outside the crater because most of the ejecta never escaped the crater cavity. A computed tomography scan of the crater showed a region of pore compaction approximately one crater radius below the crater. *Housen et al.* (1999) and *Housen and Holsapple* (2003) also impacted one of the used targets close to the original crater and confirmed that there was little interaction between the craters. For example, the first crater did not collapse as a result of the second impact, nor was the first crater erased as a result of shaking or ejecta filling in the first crater.

The authors conclude that large impacts onto compressible, highly porous targets may not reach the gravity regime in which the gravity scaling laws can be employed to predict crater diameter and depth. In Plate 3, the compaction craters in perlite and mixtures of sand, perlite and fly ash (open symbols) are strength-dominated. As a result, a porous, compressible object may have a very high resistance to disruption even if both the tensile and compressive strengths are low.

The occurrence of compaction cratering in nature is not understood and presently a subject of debate. More work on the compaction cratering phenoma is needed. If compaction cratering is prevalent, the bulk density of a porous compressible object may be significantly increased over the age of the solar system by compaction from impacts.

5.1.4. Cratering in other volatile materials. Kuiper belt objects show wide diversity in volatile content. Large KBOs that are bright enough for detailed spectroscopic study show evidence of significant volatile content (e.g., methane and ethane ices) (chapter by Barucci et al.; *Brown et al.,* 2007a; *Barucci et al.,* 2005). Laboratory experiments have found that the addition of material more volatile than H_2O ice, such as CO_2 and NH_3 (*Burchell et al.,* 1998; *Burchell and Johnson,* 2005; *Schultz,* 1996), can increase the strength of the target and, as a result, decrease the cratering efficiency.

The phase of the volatile is also important. Comet nuclei and their precursors may contain trapped pockets of gas under high internal pressures. If an impact event releases trapped gas, the vapor expansion may aid in the ejection of more mass than would be possible from the kinetic energy of the impact itself (*Durda et al.,* 2003; *Schultz et al.,* 2005; *Holsapple and Housen,* 2007).

5.1.5. Cratering in layered targets. *Belton et al.* (2007) suggest that all three Jupiter-family-comet nuclei (believed to originate in the scattered disk component of the Kuiper belt) that have been closely observed to date (Wild 2, Borrelly, and Tempel 1) show evidence of layering. *Belton et al.* (2007) propose that this layering is primordial and a result of the accretion process. By extrapolation, the precursor objects in the Kuiper belt may also have layered structures. Whether the observed layering is primordial or not is a matter of debate; however, surface layering (a devolatilized "crust") was predicted for comets based on thermal evolution models (*Belton and A'Hearn,* 1999). Layering of different strength materials does explain features seen on other objects in the solar system. For example, concentric crater morphology on the Moon and slightly filled in linear structures on the asteroid Eros can be explained by regolith overlying more competent rock.

Oberbeck and Quaide (1967) and *Ryan et al.* (1991) conducted experiments on regolith-covered targets and determined that the morphology of the resulting crater changed depending on the depth of the regolith. This result has been confirmed with numerical experiments by *Senft and Stewart* (2007). *Ryan et al.* (1991) conducted drop tests to study the collision outcome of aggregate projectiles impacting different depths of regolith (fine particles overlaying a concrete surface). When the depth of the regolith was at least the size of the projectile, the aggregate lost <10% of its mass when dropped from a height that resulted in catastophic disruption when the surface was not covered with a layer of fine particles. The porous regolith was very efficient at dissipating the impact energy.

In addition, impact experiments into granular mixtures of H_2O ice, CO_2 ice, and pyrophylite that have experienced thermal stratification produce craters with very different morphologies (*Arakawa et al.,* 2000). Finally, *Schultz* (2003) looked at the effect of layering on crater scaling. Craters retain their original diameter until the layer becomes less than twice the projectile diameter (for vertical impacts) or less than a projectile diameter (for oblique impacts). Even though the final crater depth is limited by the substrate, the

diameter remains unaffected. Imagery of craters on the surfaces of KBOs would provide information about near-surface layering.

5.2. Catastrophic Disruption

As mentioned above, there has been much less work in the catastrophic disruption regime than the cratering regime. We begin this section with a brief summary of the laboratory experiments of catastrophic disruption either using ice targets or investigating a range of porosities. Next, numerical experiments on ice or porous targets are presented.

5.2.1. Catastrophic disruption laboratory experiments. Strength-regime laboratory experiments have investigated the catastrophic disruption of icy and porous targets. Both *Love et al.* (1993) and *Ryan et al.* (1999) conducted catastrophic disruption impact experiments into macroporous targets. *Arakawa et al.* (2002) performed impact experiments into nonporous and porous pure ice and ice silicate mixtures. In most of the experiments, the porous targets were more difficult to disrupt because the kinetic energy of the projectile is partitioned into crushing energy to fill void spaces (*Love et al.,* 1993) and the shock wave reflects off the large number of free surfaces. The result is significant attenuation of the shock wave compared to solid materials.

Ryan et al. (1999) conducted 20 low-speed (100 m s^{-1}) impact experiments into solid and porous ice targets. They found that porous ice targets, although significantly weaker than the solid ice targets under static conditions, had a disruption strength equivalent to the solid targets with similar total mass. The authors attribute this behavior to the efficient dissipation of energy in void spaces.

Love et al. (1993) ran a series of hypervelocity experiments (4.8–6.0 km s^{-1}) into glass targets of varying porosity and strength. They found that the specific energy needed to catastrophically disrupt the target was proportional to (1-porosity)$^{-3.6}$. Their results suggest that the porosity of the target is more important for the collision outcome than the compressive strength of the target. More work is needed to separate the effects of porosity and strength. Impacts into the more porous targets resulted in deeper penetration of the projectile but the excavated volume was about the same as in less porous targets. With higher porosity, the damage from the impact was more localized. These results suggest that porous objects in the solar system would have longer lifetimes against collisional disruption than monoliths of the same material.

Arakawa et al. (2002) performed moderate-speed impact experiments (150–670 m s^{-1}) into ice and ice-silicate mixtures to quantify the effect of porosity on disruption strength. In pure ice targets, the disruption strength increased with increasing porosity. Puzzlingly, in mixed material targets, the disruption strength decreased with increasing porosity. These experiments suggest that the nature of the material bonding (and material strength) can be as important as the bulk porosity.

The work to date demonstrates that porosity plays a significant role in the outcome of catastrophic disruption experiments. However, more work is needed to understand how porosity strengthens a material and how to predict disruption strength as a function of porosity.

5.2.2. Catastrophic disruption numerical simulations. Investigations of catastrophic disruption in the gravity regime rely upon numerical experiments. Studies including KBO analog materials are limited. *Asphaug et al.* (1998) have considered km s^{-1} impacts into macroporous targets. *Benz and Asphaug* (1999) and Leinhardt and Stewart (in preparation) have studied the disruption of solid ice targets. More complex simulations of KBOs including microporosity and mixed silicates with ice have yet to be conducted.

Using a SPH code, *Asphaug et al.* (1998) investigated how different internal configurations affect the collision outcome. They considered 5 km s^{-1} rocky impacts onto a target shaped like asteroid Castalia, which appears to be a contact binary. The possible internal structures considered were (1) a solid rock, (2) a global rubble pile with 50% bulk porosity, and (3) two solid rock pieces separated by a zone of highly damaged rock. In all three cases, the mass of the target was constant (the density of the rock was changed). The model included material strength and self-gravity.

In the rubble-pile case, some of the energy generated by the impact is partitioned into collapsing void space. In addition, the shock wave reflects off the free surfaces of the rubble pieces. As a result, shock effects were focused close to the impact site and the shock pressures were dissipated much more quickly compared to the solid rock target, in agreement with laboratory impact experiments (section 5.2.1). The velocities of the ejected material were higher in the rubble-pile configuration than the solid-rock case, resulting in a small ejecta blanket or none at all. In the two-solid-piece model, the damaged region in the middle of the body reflects the shock wave so that the damage is localized to the piece that was impacted. This study elegantly demonstrates the importance of internal structure in the outcome of collision events.

A significant problem limiting numerical studies of hypervelocity catastrophic disruption events is the vast difference in dynamical times between the shock propagation and gravitational reaccumulation. To make the problem more tractable, Leinhardt and Stewart (in preparation) have begun using a hybridized shock physics–gravity method to study KBO analog objects (Plate 4). The impact and deformation stage is modeled using a shock-physics code, CTH (*McGlaun et al.,* 1990), and the results are handed to a N-body gravity code, pkdgrav (*Stadel,* 2001; *Richardson et al.,* 2000; *Leinhardt et al.,* 2000). This method allows detailed modeling of the shock deformation including heating, phase changes, and mixing of material as well as the final gravitational reaccumulation of fragments.

These simulations record the provenance of the material in the largest remnants and track the degree to which the reaccumulated material is processed by the initial impact event. For example, the peak shock pressure (and hence the amount of melting or vaporization) experienced by each mass element is recorded. In a catastrophic impact, a large fraction of the original surface is lost, and the original surface of the target is only maintained at the antipode of the largest postcollision remnant. The surface materials on the

largest remnant reflect heterogeneous shock processing (Plate 4). Both highly and weakly shocked material lines the surface, while the interior material has a more homogeneous history of moderate shock levels. This suggests that the surface materials on KBOs that have suffered a catastrophic impacts could be heterogeneously devolatilized in comparison to the interior. The surface heterogeneity may also lead to color variations.

6. SUMMARY AND FUTURE DIRECTIONS

In this chapter, we have discussed the present state of knowledge about the possible physical effects of collisions in the Kuiper belt. The body of work on impact cratering and disruption events in KBO analog materials demonstrate that composition and internal structure (particularly porosity) have a significant affect on the final outcome of collision events. Understanding the role of collisions in changing the composition and structure of KBOs is important because KBOs are the best representatives of the planetesimals that accreted into the outer solar system planets.

The range of possible outcomes of collisions in the Kuiper belt region is more complicated than in the asteroid belt. In particular, the low relative impact velocities, the low mean density of KBOs, and the likely presence of a variety of internal structures are not fully accounted for in present impact models. Impact cratering scaling laws and catastrophic disruption criteria that have been developed for hypervelocity collisions on solid planetary surfaces and within the asteroid belt may not be widely applicable to KBOs. For example, the unanticipated large amount of mass ejected from Comet Tempel 1 from the Deep Impact mission revealed that important physical processes are missing from the crater scaling laws (*Holsapple and Housen,* 2007).

We close with recommendations for areas of future work to advance our knowledge of the properties of KBOs:

1. What is the role of porosity in the outcome of cratering and catastrophic disruption collisions? And how do we separate the effects of porosity and strength? Predicting the outcome of collisions into porous materials of various strengths requires an improved understanding of (a) energy coupling into the target and (b) shock-induced damage (degradation of strength). As both are difficult to model accurately in codes, clever laboratory experiments that include direct measurements of shock wave decay, damage, and final crater sizes, in targets that vary porosity and strength independently, are necessary. In cratering events, the residual strength of the damaged target ultimately determines the final crater shape and the transition between strength- and gravity-dominated regimes. For disruption events, laboratory results will need to be incorporated into numerical simulations.

2. What is the correct way to scale laboratory experiments on porous materials to larger scales? Two length scales appear to dominate the problem: (a) the length scale of the porosity with respect to the deforming shock wave (microporosity vs. macroporosity), and (b) the depth of energy coupling of the projectile. Laboratory and numerical experiments can directly address the effects of varying each length scale as the problem size increases from laboratory targets to planets. More information about the scale of porosities in KBOs can be obtained from studies of comet nuclei and inferences of rubble pile vs. differentiated internal structures in large KBOs.

3. How should volatility be incorporated into scaling laws? Vapor generation (or release) from a collision event would affect the momentum of the flow of excavated or dispersed material. This difficult problem requires more information on the actual composition of KBOs.

4. How does differentiation or layering affect the catastrophic disruption threshold? The propagation of the impact shock wave through the target is influenced by a layered internal structure. This tractable problem can be addressed through laboratory and numerical experiments of plausible internal configurations in KBOs.

5. How does the mass ratio of the colliding bodies change the catastrophic disruption criteria in the hypervelocity regime? The shock pressure profile through the target depends on the size and velocity of the projectile. Laboratory and numerical experiments can directly address this problem for solid bodies. Solutions to the first question in this list are required for highly porous bodies.

6. How can we validate numerical simulations in the gravity regime? Crater scaling laws have been validated by high-gravity (centrifuge) experiments. In the study of highly porous and weak materials, experiments in vacuum and under low gravity are also needed. Validation of catastrophic disruption simulations in the gravity regime will require new techniques.

7. What is the magnitude of modifications of KBOs from mutual collisions compared to other "weathering" processes? How different are present-day KBOs from the primordial planetesimals in the outer solar system? Cumulative changes in observable properties of KBOs, including densities, colors, composition, and internal structures, can be addressed by updating collisional evolution models of the Kuiper belt with the latest understanding of collisional processes in porous, icy bodies. Given the wide range of possible physical properties of KBOs, studies of individual collisions are warranted to examine common impact scenarios. At present there is no certain answer, and our understanding will be driven by observations to come.

Acknowledgments. The authors thank K. Housen, S. Kenyon, and E. Asphaug for careful review of this manuscript. We would also like to thank A. Morbidelli, L. Senft, M. Holman, J.-L. Margot, M. Brown, E. Schaller, and D. Raggozine for helpful discussions.

REFERENCES

Ahrens T. J. and Johnson M. L. (1995a) Shock wave data for minerals. In *Mineral Physics and Crystallography, A Handbook of Physical Constants, Vol. 2* (T. J. Ahrens, ed.), pp. 143–184. American Geophysical Union, Washington, DC.

Ahrens T. J. and Johnson M. L. (1995b) Shock wave data for rocks.

In *Rock Physics and Phase Relations, A Handbook of Physical Constants, Vol. 3* (T. J. Ahrens, ed.), pp. 35–44. American Geophysical Union, Washington, DC.

Ahrens T. J. and O'Keefe J. D. (1977) Equations of state and impact-induced shock-wave attenuation on the Moon. In *Impact and Explosion Cratering: Planetary and Terrestrial Implications* (D. J. Roddy et al., eds.), pp. 639–656. Pergamon, New York.

Ahrens T. J. and O'Keefe J. D. (1987) Impact on the Earth, ocean and atmosphere. *Intl. J. Impact Eng., 5,* 13–32.

Arakawa M., Higa M., Leliwa-Kopystyński J., and Maeno N. (2000) Impact cratering of granular mixture targets made of H_2O ice-CO_2 ice-pyrophylite. *Planet. Space Sci., 48,* 1437–1446.

Arakawa M., Leliwa-Kopystyński J., and Maeno N. (2002) Impact experiments on porous icy-silicate cylindrical blocks and the implication for disruption and accumulation of small icy bodies. *Icarus, 158,* 516–531.

Asphaug E., Ostro S. J., Hudson R. S., Scheeres D. J., and Benz W. (1998) Disruption of kilometre-sized asteroids by energetic collisions. *Nature, 393,* 437–440.

Asphaug E., Ryan E. V., and Zuber M. T. (2002) Asteroid interiors. In *Asteroids III* (W. F. Bottke Jr. et al., eds.), pp. 463–484. Univ. of Arizona, Tuscon.

Barucci M. A., Cruikshank D. P., Dotto E., Merlin F., Poulet F., Dalle Ore C., Fornasier S., and de Bergh C. (2005) Is Sedna another Triton? *Astron. Astrophys., 439,* L1–L4.

Belton M. J. S. and A'Hearn M. F. (1999) Deep sub-surface exploration of cometary nuclei. *Adv. Space Res., 24,* 1175–1183.

Belton M. J. S., Thomas P., Veverka J., Schultz P., A'Hearn M. F., Feaga L., Farnham T., Groussin O., Li J. Y., Lisse C., McFadden L., Sunshine J., Meech K. J., Delamere W. A., and Kissel J. (2007) The internal structure of Jupiter family cometary nuclei from Deep Impact observations: The "talps" or "layered pile" model. *Icarus, 187,* 332.

Bendjoya P. and Zappalà V. (2002) Asteroid family identification. In *Asteroids III* (W. F. Bottke Jr. et al., eds.), pp. 613–618. Univ. of Arizona, Tuscon.

Benz W. and Asphaug E. (1999) Catastrophic disruptions revisited. *Icarus, 142,* 5–20.

Bernstein G. M., Trilling D. E., Allen R. L., Brown M. E., Holman M., and Malhotra R. (2004) The size distribution of trans-neptunian bodies. *Astron. J., 128,* 1364–1390.

Brown M. E., Barkume K. M., Blake G. A., Schaller E. L., Rabinowitz D. L., Roe H. G., and Trujillo C. A. (2007a) Methane and ethane on the bright Kuiper belt object 2005 FY9. *Astron. J., 133,* 284–289.

Brown M. E., Barkume K. M., Ragozzine D., and Schaller E. L. (2007b) A collisional family of icy objects in the Kuiper belt. *Nature, 446,* 231–346.

Burchell M. J. and Johnson E. (2005) Impact craters on small icy bodies such as icy satellites and comet nuclei. *Mon. Not. R. Astron. Soc., 360,* 769–781.

Burchell M. J., Brooke-Thomas W., Leliwa-Kopystyński J., and Zarnecki J. C. (1998) Hypervelocity impact experiments on solid CO_2 targets. *Icarus, 131,* 210–222.

Burchell M. J., Johnson E., and Grey I. D. S. (2002) Hypervelocity impacts on porous ices. In *Asteroids, Comets, and Meteors: ACM 2002* (B. Warmbein, ed.), pp. 859–862. ESA SP-500, Noordwijk, The Netherlands.

Chapman C. R. and McKinnon W. B. (1986) Cratering of planetary satellites. In *Satellites* (J. A. Burns and M. S. Matthews, eds.), pp. 492–580. Univ. of Arizona, Tuscon.

Chen W. P., Alcock C., Axelrod T., Bianco F. B., Byun Y. I., Chang Y. H., Cook K. H., Dave R., Giammarco J., Kim D. W., King S. K., Lee T., Lehner M., Lin C. C., Lin H. C., Lissauer J. J., Marshall S., Meinshausen N., Mondal S., de Pater I., Porrata R., Rice J., Schwamb M. E., Wang A., Wang S. Y., Wen C. Y., and Zhang Z. W. (2006) Search for small trans-neptunian objects by the TAOS Project. In *Near-Earth Objects, Our Celestial Neighbors: Opportunity and Risk* (A. Milani et al., eds.), pp. 65–68. IAU Symposium 236, Cambridge Univ., Cambridge.

Cintala M. J., Smrekar S., Hörz F., and Cardenas F. (1985) Impact experiments in H_2O ice, I: Cratering (abstract). In *Lunar and Planetary Science XVI,* pp. 131–132. Lunar and Planetary Institute, Houston.

Croft S. K., Kieffer S. W., and Ahrens T. J. (1979) Low-velocity impact craters in ice and ice-saturated sand with implications for martian crater count ages. *J. Geophys. Res., 84,* 8023–8032.

Davis D. R. and Farinella P. (1997) Collisional evolution of Edgeworth-Kuiper belt objects. *Icarus, 125,* 50–60.

Davis D. R., Chapman C. R., Greenberg R., Weidenschilling S. J., and Harris A. W. (1979) Collisional evolution of asteroids — Populations, rotations, and velocities. In *Asteroids* (T. Gehrels, ed.), pp. 528–557. Univ. of Arizona, Tuscon.

Dell'Oro A., Marzari F., Paolicchi P., and Vanzani V. (2001) Updated collisional probabilities of minor body populations. *Astron. Astrophys., 366,* 1053–1060.

dell'Oro A., Paolicchi P., Cellino A., Zappalà V., Tanga P., and Michel P. (2001) The role of families in determining collision probability in the asteroid main belt. *Icarus, 153,* 52–60.

Dohnanyi J.W. (1969) Collisional models of asteroids and their debris. *J. Geophys. Res., 74,* 2531–2554.

Durda D. D., Flynn G. J., and van Veghten T. W. (2003) Impacts into porous foam targets: Possible implications for the disruption of comet nuclei. *Icarus, 163,* 504–507.

Fujiwara A., Kawaguchi J., Yeomans D. K., Abe M., Mukai T., Okada T., Saito J., Yano H., Yoshikawa M., Scheeres D. J., Barnouin-Jha O., Cheng A. F., Demura H., Gaskell R. W., Hirata N., Ikeda H., Kominato T., Miyamoto H., Nakamura A. M., Nakamura R., Sasaki S., and Uesugi K. (2006) The rubble-pile asteroid Itokawa as observed by Hayabusa. *Science, 312(5778),* 1330–1334.

Furnish M. D. and Remo J. L. (1997) Ice issues, porosity, and snow experiments for dynamic NEO and comet medeling. In *Near-Earth Objects: The United Nations International Conference* (J. L. Remo, ed.), pp. 566–582. New York Academy of Science, New York.

Grey I. D. S. and Burchell M. J. (2003) Hypervelocity impact cratering on water ice targets at temperatures ranging from 100 K to 253 K. *J. Geophys. Res., 108,* 6-1.

Gross J., Reichenauer G., and Fricke J. (1988) Mechanical-properties of SiO_2 aerogels. *J. Phys. D, 21(9),* 1447–1451.

Gurnett D. A., Ansher J. A., Kurth W. S., and Granroth L. J. (1997) Micron-sized dust particles detected in the outer solar system by the Voyager 1 and 2 plasma wave instruments. *Geophys. Res. Lett., 24,* 3125–3128.

Hahn J. M. and Malhotra R. (1999) Orbital evolution of planets embedded in a planetesimal disk. *Astron. J., 117,* 3041–3053.

Herrmann W. (1969) Constitutive equation for the dynamic compaction of ductile porous materials. *J. Appl. Phys., 40(6),* 2490–2499.

Holsapple K. A. (1987) The scaling of impact phenomenon. *Intl. J. Impact Eng., 5,* 343–355.

Holsapple K. A. (1993) The scaling of impact processes in plane-

tary sciences. *Annu. Rev. Earth Planet. Sci., 21,* 333–373.
Holsapple K. A. (2007) Spin limits of solar system bodies: From the small fast-rotators to 2003 EL61. *Icarus, 187,* 500–509.
Holsapple K. A. and Housen K. R. (2004) The cratering database: Making code jockeys honest (abstract). In *Lunar and Planetary Science XXXV,* Abstract #1779. Lunar and Planetary Institute, Houston (CD-ROM).
Holsapple K. A. and Housen K. R. (2007) A crater and its ejecta: An interpretation of deep impact. *Icarus, 187(1),* 345.
Holsapple K. A. and Schmidt R. M. (1987) Point source solutions and coupling parameters in cratering mechanics. *J. Geophys. Res., 92,* 6350–6376.
Holsapple K., Giblin I., Housen K., Nakamura A., and Ryan E. (2002) Asteroid impacts: Laboratory experiments and scaling laws. In *Asteroids III* (W. F. Bottke Jr. et al., eds.), pp. 443–462. Univ. of Arizona, Tucson.
Housen K. R. and Holsapple K. A. (1999) Scale effects in strength-dominated collisions of rocky asteroids. *Icarus, 142(1),* 21–33.
Housen K. R. and Holsapple K. A. (2000) Numerical simulations of impact cratering in porous materials (abstract). In *Lunar and Planetary Science XXXI,* Abstract #1498. Lunar and Planetary Institute, Houston.
Housen K. R. and Holsapple K. A. (2003) Impact cratering on porous asteroids. *Icarus, 163,* 102–119.
Housen K. R., Holsapple K. A., and Voss M. E. (1999) Compaction as the origin of the unusual craters on the asteroid Mathilde. *Nature, 402,* 155–157.
Humes D. H. (1980) Results of Pioneer 10 and 11 meteoroid experiments — Interplanetary and near-Saturn. *J. Geophys. Res., 85,* 5841–5852.
Iijima Y. i., Kato M., Arakawa M., Maeno N., Fujimura A., and Mizutani H. (1995) Cratering experiments on ice: Dependence of crater formation on projectile materials and scaling parameter. *Geophys. Res. Lett., 22,* 2005–2008.
Jeanloz R. (1989) Shock wave equation of state and finite strain theory. *J. Geophys. Res., 94(B5),* 5873–5886.
Jewitt D. C. and Luu J. X. (2000) Physical nature of the Kuiper belt. In *Protostars and Planets IV* (V. Mannings et al., eds.), pp. 1201–1230. Univ. of Arizona, Tucson.
Johnson J. B. (1991) Simple model of shock-wave attenuation in snow. *J. Glaciol., 37(127),* 303–312.
Kato M., Iijima Y., Arakawa M., Okimura Y., Fujimura A., Maeno N., and Mizutani H. (1995) Ice-on-ice impact experiments. *Icarus, 113,* 423–441.
Kawakami S., Mizutani H., Takagi Y., Kato M., and Kumazawa M. (1983) Impact experiments on ice. *J. Geophys. Res., 88,* 5806–5814.
Kenyon S. J. and Bromley B. C. (2004) The size distribution of Kuiper belt objects. *Astron. J., 128,* 1916–1926.
Kenyon S. J. and Luu J. X. (1999) Accretion in the early Kuiper belt. II. Fragmentation. *Astron. J., 118,* 1101–1119.
Koschny D. and Grün E. (2001) Impacts into ice-silicate mixtures: Crater morphologies, volumes, depth-to-diameter ratios, and yield. *Icarus, 154,* 391–401.
Koschny D., Kargl G., and Rott M. (2001) Experimental studies of the cratering process in porous ice targets. *Adv. Space Res., 28,* 1533–1537.
Lacerda P. and Jewitt D. (2007) Densities of solar system objects from their rotational lightcurves. *Astron. J.,* in press.
Landgraf M., Liou J. C., Zook H. A., and Grün E. (2002) Origins of solar system dust beyond Jupiter. *Astron. J., 123,* 2857–2861.
Lange M. A. and Ahrens T. J. (1982) Impact cratering in ice and ice-silicate targets: An experimental assessment (abstract). In *Lunar and Planetary Science XIII,* pp. 415–416. Lunar and Planetary Institute, Houston.
Lange M. A. and Ahrens T. J. (1983) The dynamic tensile strength of ice and ice silicate mixtures. *J. Geophys. Res., 88,* 1197–1208.
Lange M. A. and Ahrens T. J. (1987) Impact experiments in low-temperature ice. *Icarus, 69,* 506–518.
Leinhardt Z. M. and Richardson D. C. (2002) N-body simulations of planetesimal evolution: Effect of varying impactor mass ratio. *Icarus, 159,* 306–313.
Leinhardt Z. M., Richardson D. C., and Quinn T. (2000) Direct N-body simulations of rubble pile collisions. *Icarus, 146,* 133–151.
Love S. G. and Ahrens T. J. (1997) Origin of asteroid rotation rates in catastrophic impacts. *Nature, 386,* 154–156.
Love S. G., Hörz F., and Brownlee D. E. (1993) Target porosity effects in impact cratering and collisional disruption. *Icarus, 105,* 216–224.
Margot J. L. (2002) Astronomy: Worlds of mutual motion. *Nature, 416,* 694–695.
McGlaun J. M., Thompson S. L., and Elrick M. G. (1990) CTH: A 3-Dimensional Shock-Wave Physics Code. *Intl. J. Imp. Eng., 10,* 351–360.
Mellor M. (1975) A review of basic snow mechanics. In *Snow Mechanics, Proceedings of the Grindelwald Symposium,* pp. 251–291. IAHS Publ. No. 114, Oxfordshire, UK.
Melosh H. J. (1977) Crater modification by gravity — A mechanical analysis of slumping. In *Impact and Explosion Cratering: Planetary and Terrestrial Implications* (D. J. Roddy et al., eds.), pp. 1245–1260. Pergamon, New York.
Melosh H. J. (1989) *Impact Cratering.* Oxford Univ., New York.
Melosh H. J. and Ivanov B. A. (1999) Impact crater collapse. *Annu. Rev. Earth Planet. Sci., 27,* 385–415.
Melosh H. J. and McKinnon W. B. (1978) The mechanics of ringed basin formation. *Geophys. Res. Lett., 5,* 985–988.
Melosh H. J. and Ryan E. V. (1997) Asteroids: Shattered but not dispersed. *Icarus, 129,* 562–564.
Merk R. and Prialnik D. (2006) Combined modeling of thermal evolution and accretion of trans-neptunian objects — Occurrence of high temperatures and liquid water. *Icarus, 183,* 283–295.
Meyers M. A. (2001) *Dynamic Behavior of Materials.* Wiley, New York.
Müller T. G., Ábrahám P., and Crovisier J. (2005) Comets, asteroids and zodiacal light as seen by ISO. *Space Sci. Rev., 119,* 141–155.
Oberbeck V. R. and Quaide W. L. (1967) Estimated thickness of a fragmental surface layer of Oceanus Procellarum. *J. Geophys. Res., 72,* 4697–4704.
O'Brien D. P. and Greenberg R. (2003) Steady-state size distributions for collisional populations: Analytical solution with size-dependent strength. *Icarus, 164(2),* 334.
O'Brien D. P. and Greenberg R. (2005) The collisional and dynamical evolution of the main-belt and NEA size distributions. *Icarus, 178,* 179–212.
Pan M. and Sari R. (2005) Shaping the Kuiper belt size distribution by shattering large but strengthless bodies. *Icarus, 173,* 342–348.
Paolicchi P., Burns J. A., and Weidenschilling S. J. (2002) Side effects of collisions: Spin rate changes, tumbling rotation states,

and binary asteroids. In *Asteroids III* (W. F. Bottke Jr. et al., eds.), pp. 517–526. Univ. of Arizona, Tucson.

Petit J. M., Holman M. J., Gladman B. J., Kavelaars J. J., Scholl H., and Loredo T. J. (2006) The Kuiper belt luminosity function from m_R = 22 to 25. *Mon. Not. R. Astron. Soc., 365,* 429–438.

Petrenko V. F. and Whitworth R. W. (1999) *The Physics of Ice.* Oxford Univ., New York.

Pierazzo E. and Melosh H. J. (2000) Melt production in oblique impacts. *Icarus, 145,* 252–261.

Pierazzo E., Vickery A. M., and Melosh H. J. (1997) A reevaluation of impact melt production. *Icarus, 127,* 408–423.

Poirier J. P. (2000) *Introduction to the Physics of the Earth's Interior.* Cambridge Univ., New York.

Rabinowitz D. L., Barkume K., Brown M. E., Roe H., Schwartz M., Tourtellotte S., and Trujillo C. (2006) Photometric observations constraining the size, shape, and albedo of 2003 EL61, a rapidly rotating, Pluto-sized object in the Kuiper belt. *Astrophys. J., 639,* 1238–1251.

Rice M. H., McQueen R. G., and Walsh J. M. (1958) Compression of solids by strong shock waves. *Solid State Phys., 6,* 1–63.

Richardson D. C., Quinn T., Stadel J., and Lake G. (2000) Direct large-scale N-body simulations of planetesimal dynamics. *Icarus, 143,* 45–59.

Roques F., Doressoundiram A., Dhillon V., Marsh T., Bickerton S., Kavelaars J. J., Moncuquet M., Auvergne M., Belskaya I., Chevreton M., Colas F., Fernandez A., Fitzsimmons A., Lecacheux J., Mousis O., Pau S., Peixinho N., and Tozzi G. P. (2006) Exploration of the Kuiper belt by high-precision photometric stellar occultations: First results. *Astron. J., 132,* 819–822.

Ruoff A. L. (1967) Linear shock-velocity-particle-velocity relationship. *J. Appl. Phys., 38(13),* 4976–4980.

Ryan E. V., Hartmann W. K., and Davis D. R. (1991) Impact experiments. III — Catastrophic fragmentation of aggregate targets and relation to asteroids. *Icarus, 94,* 283–298.

Ryan E. V., Davis D. R., and Giblin I. (1999) A laboratory impact study of simulated Edgeworth-Kuiper belt objects. *Icarus, 142,* 56–62.

Sammonds P. R., Murrell S. A. F., and Rist M. A. (1998) Fracture of multiyear sea ice. *J. Geophys. Res., 103(C10),* 21795–21815.

Schmidt R. M. (1980) Meteor Crater: Energy of formation — Implications of centrifuge scaling (abstract). In *Lunar and Planetary Science XI,* pp. 2099–2128. Lunar and Planetary Institute, Houston.

Schultz P. H. (1996) Effect of impact angle on vaporization. *J. Geophys. Res., 101,* 21117–21136.

Schultz P. H. (2003) Impacts into porous volatile-rich substrates on Mars (abstract). In *Sixth International Conference on Mars,* Abstract #3263. Lunar and Planetary Institute, Houston (CD-ROM).

Schultz P. H. and Gault D. E. (1985) Clustered impacts — Experiments and implications. *J. Geophys. Res., 90,* 3701–3732.

Schultz P. H., Ernst C. M., and Anderson J. L. B. (2005) Expectations for crater size and photometric evolution from the Deep Impact collision. *Space Sci. Rev., 117,* 207–239.

Senft L. E. and Stewart S. T. (2007) Modeling impact cratering in layered surfaces. *J. Geophys. Res., 112,* E11002, DOI: 10.1029/2007JE002894.

Shrine N. R. G., Burchell M. J., and Grey I. D. S. (2002) Velocity scaling of impact craters in water ice over the range 1 to 7.3 km s^{-1}. *Icarus, 155,* 475–485.

Stadel J. G. (2001) Cosmological N-body simulations and their analysis. Ph.D. thesis. Univ. of Washington, Seattle. 141 pp.

Stern S. A. (1996) On the collisional environment, accretion time scales, and architecture of the massive, primordial Kuiper belt. *Astron. J., 112,* 1203–1211.

Stern S. A. (2003) The evolution of comets in the Oort cloud and Kuiper belt. *Nature, 424,* 639–642.

Stern S. A. and Colwell J. E. (1997) Collisional erosion in the primordial Edgeworth-Kuiper belt and the generation of the 30–50 AU Kuiper gap. *Astrophys. J., 490,* 879–882.

Stewart S. T. and Ahrens T. J. (2004) A new H_2O Ice Hugoniot: Implications for planetary impact events. In *Shock Compression of Condensed Matter — 2003* (M. D. Furnish et al., ed.), pp. 1478–1483. American Institute of Physics, New York.

Stewart S. T. and Ahrens T. J. (2005) Shock properties of H_2O ice. *J. Geophys. Res., 110(E9),* 3005.

Strom R. G., Malhotra R., Ito T., Yoshida F., and Kring D. A. (2005) The origin of planetary impactors in the inner solar system. *Science, 309,* 1847–1850.

Trujillo C. A., Jewitt D. C., and Luu J. X. (2001) Properties of the trans-neptunian belt: Statistics from the Canada-France-Hawaii Telescope Survey. *Astron. J., 122,* 457–473.

Veverka J., Thomas P., Harch A., Clark B., Bell J. F. III, Carcich B., Joseph J., Chapman C., Merline W., Robinson M., Malin M., McFadden L. A., Murchie S., Hawkins S. E. III, Farquhar R., Izenberg N., and Cheng A. (1997) NEAR's flyby of 253 Mathilde: Images of a C asteroid. *Science, 278,* 2109–2114.

Weissman P. R., Asphaug E., and Lowry S. C. (2005) Structure and density of cometary nuclei. In *Comets II* (M. C. Festou et al., eds.), pp. 337–357. Univ. of Arizona, Tuscon.

Williams D. R. and Wetherill G. W. (1994) Size distribution of collisionally evolved asteroidal populations: Analytical solution for self-similar collision cascades. *Icarus, 107(1),* 117.

Wünnemann K., Collins G. S., and Melosh H. J. (2006) A strain-based porosity model for use in hydrocode simulations of impacts and implications for transient crater growth in porous targets. *Icarus, 180,* 514–527.

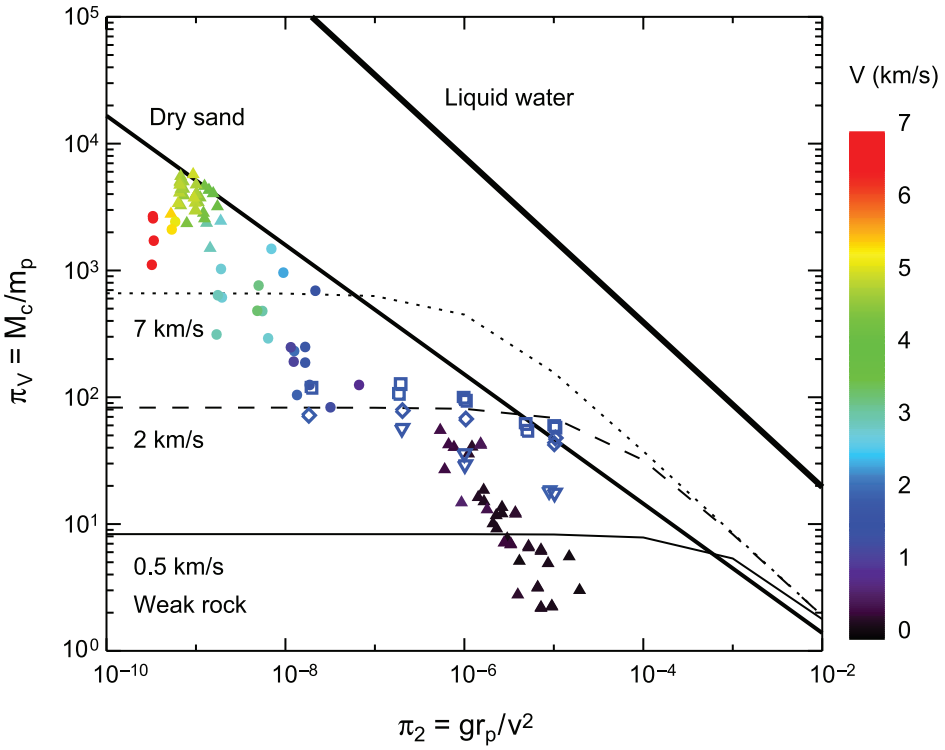

Plate 3. Cratering efficiencies (ratio of ejected and displaced mass to projectile mass, p_V) as a function of the ratio of gravitational to inertial forces (inverse Froude number, p_2) for different target materials at different velocities. Lines denote fitted cratering efficiencies in liquid water, dry sand (35% porosity), and weak rock using equation (10). Experimental data (see text): nonporous ice, ▲; 50% porous ice, ●; various crushable nonicy mixtures with porosities of about 40%, □; 70%, ◇; and 96%, ▽. Colors denote impact velocity.

Accompanies chapter by Leinhardt et al. (pp. 195–211).

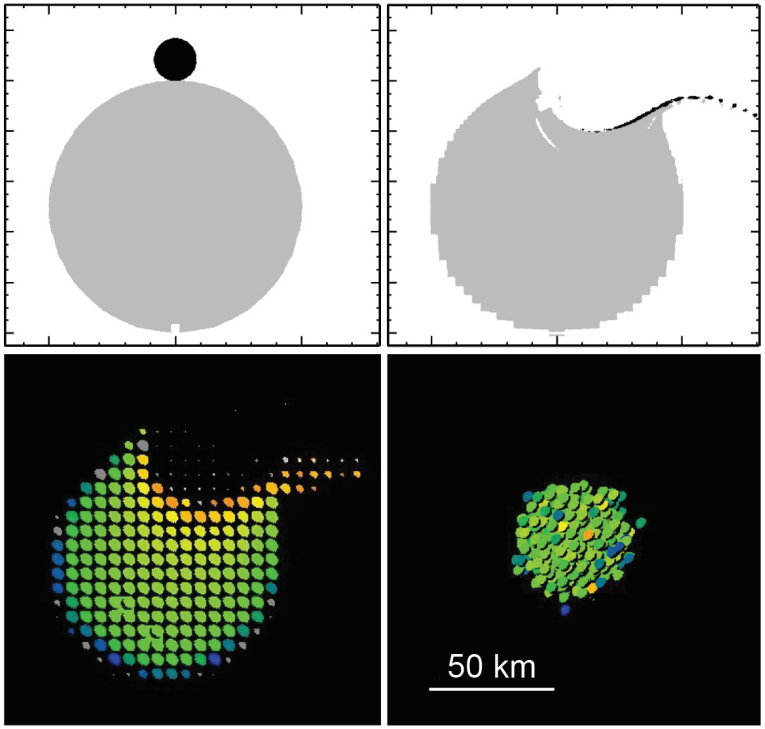

Plate 4. An example of a hybrid hydrocode to N-body numerical simulation of the catastrophic disruption of a solid ice target. The first row shows the positions of the target (gray) and projectile (black) at time 0 and 30 s. The second row shows the target after handoff from the hydrocode to the N-body code at 60 s and the largest remnant (r = 35 km) at 140 h. The projectile (r = 8.4 km) hit the target (r = 50 km) at 45° and 3 km s^{-1}. The first three frames show a slice through the three-dimensional target and projectile along the y = 0 plane. The final frame shows the surface of the largest postcollision remnant. The color coding in the N-body frames show the peak pressure attained by each mass element. Blue is the lowest peak pressure (2×10^6 dynes cm^{-2}), and red is the highest (1×10^{11} dynes cm^{-2}). The peak pressure is stored in Lagrangian tracer particles during the hydrocode component of the simulation. The few noncolored (gray or white) particles in the N-body images are blocks from the hydrocode grid that did not contain any tracer particles. The surface of the largest remnant shows a mixture of high and low levels of shock deformation.

Accompanies chapter by Leinhardt et al. (pp. 195–211).